Journal of Materials Chemistry A

Accepted Manuscript

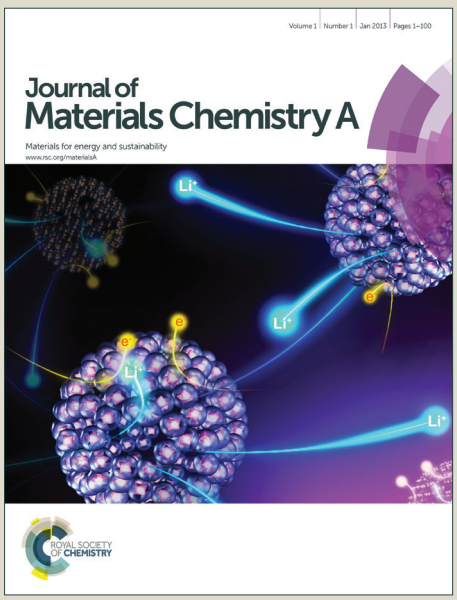

ROYAL SOCIETY OF CHEMISTRY

www.rsc.org/materialsA

Mesostructured Alumina as Powders and Thin Films

Georg J. B. Voss,[†] Elvia A. Chavez,[‡] Anette Midttveit,[†] Jostein B. Fløystad,[¶] Kristin Høydalsvik,[¶] Alain Gibaud,[‡] Dag W. Breiby,[¶] and Magnus Rønning[*,†]

Department of Chemical Engineering, Norwegian University of Science and Technology (NTNU), Sem Sælands vei 4, 7491 Trondheim, Norway, Laboratoire P.E.C. Rayons-X, Institut des Molécules et Materiaux du Mans, Université du Maine , Avenue Olivier Messaiaen, 72085 Le Mans, France, and Department of Physics, Norwegian University of Science and Technology (NTNU), Høgskoleringen 5, 7491 Trondheim, Norway

E-mail: magnus.ronning@ntnu.no

Phone: +47 735 94121. Fax: +47 735 94080

Abstract

Mesoporous aluminas offer a wide variety of applications, including catalysis, gas sensing, optics, photovoltaics, and ion exchange. However, the pores are commonly unordered and show a wide pore size distribution, creating a need for porous aluminas with well defined, tailored pore systems. Here we report the synthesis and detailed structural studies of mesoporous alumina as thin films and as powders. The synthesis was based on evaporation-induced self-assembly (EISA) of triblock copolymers Pluronic P-123 and Pluronic F-127 as structure

[*]To whom correspondence should be addressed
[†]Department of Chemical Engineering, NTNU
[‡]Laboratoire P.E.C., Université du Maine
[¶]Department of Physics, NTNU

directing agents. Structural studies of the thin films were done by grazing incidence small-angle X-ray scattering (GISAXS) supported by numerical simulations, and X-ray reflectivity. From the quantitative GISAXS studies of the as-cast films, the unit cell dimensions, space groups and also certain details of the regular micellar shape could be retrieved, indicating that the micelles were deformed by compression along the sample normal. As-cast thin films prepared from F-127 were found to give 110-oriented body-centered cubic micellar structures, while films prepared from P-123 had hexagonally packed tubular micelles. Mesoporous powder materials with narrow pore size distribution and high surface area, as characterized by N_2 physisorption, were synthesized using the same strategy. The atomic-scale phase transformation of the powder from amorphous to crystalline takes place above 800 °C, as shown by *in situ* X-ray diffraction. Both the thin films and the powders were tailored to give mesoporous alumina with a pore size of about 5 nm.

Introduction

The discovery of mesoporous silica in 1992 [1] sparked a new research field devoted to understanding and further developing these metal oxides and their applications in industry and academia. They represent a group of nanomaterials with high surface area, often highly ordered pore geometries and monodisperse, adjustable pore sizes and are thus of interest to solid-state chemists, physicists and material scientists. In the past these metal oxides were mainly ordered silica or titania due to their thermal, chemical and mechanical stability.[2,3] Recently, the focus has been shifted towards alumina Al_2O_3 [4–6] which in particular enjoys broad applicability as a catalyst support in petroleum refinement.[7,8] However, the synthesis of ordered and thermally stable mesoporous alumina represents new challenges, with the synthesis being susceptible to hydrolysis and phase transitions, easily affected by pH, water, temperature and other factors.[9]

Previous studies report alumina with ordered pores, fabricated using self-assembly methods.[10,11] Jiang *et al.*[12] demonstrated the framework crystallization of ordered mesoporous alumina thin films to γ-alumina. However, the alumina in the framework was prepared with hydrochloric acid

as hydrolysis catalyst, which renders it less attractive for catalytic applications. Lesaint *et al.*[13] employed surfactants of the Pluronic family to synthesize alumina with exceptionally large pore sizes but without long-range order. Kuemmel *et al.*[14] reported the preparation of nanocrystalline γ-alumina layers with ordered mesoporosity using specialty templates like copolymers KLE22, which has a higher contrast between hydrophilic and hydrophobic blocks compared to the Pluronics family. However, the stability of the ordered network is based on the stability of the KLE22 template above the dehydration temperature of the inorganic phase. Weidmann *et al.*[15] used block copolymers as structure-directing agents for aluminum-oxo-hydroxo building blocks for the morphology-controlled synthesis of nanocrystalline η-alumina. The produced thin films and powders exhibited uniform pores ranging from 10 to 30 nm, but the procedure requires the synthesis of the building blocks beforehand. Nevertheless, the step from the synthesis of ordered mesoporous alumina thin films and to their powder equivalent is rarely discussed. Alumina thin films are more prone to form ordered structure at the mesoscale owing to the directing influences of both the supporting substrate and the interface to air. Powders, on the other hand form a class of materials called "organized mesoporous aluminas" (OMA), which exhibit no long-range order of the pores, but a narrow pore size distribution in the mesoporous region.[16] In general the following points are often desired for catalyst support materials: i) a narrow pore size distribution, which indicates monodisperse pores; ii) a high surface area, showing that the pores are not collapsed; and iii) a well-defined atomic-scale crystal structure. While the crystal structure is an important part of any catalyst support material, the phase transitions of alumina are affected by hydrolysis, pH, and temperature, thus interfering with the optimal conditions of the templating technique to produce organized mesopores.

Nanostructured films are often characterized by transmission electron microscopy (TEM), which must be conducted in vacuum, typically on films lifted off the substrate. Powder X-ray diffraction may be conducted on as-cast films under ambient conditions, but probes only the magnitude of the scattering vector, making it impractical to study oriented phases by this method.[17,18] An increasingly used method for thin film structure studies is grazing-incidence small-angle X-ray scattering

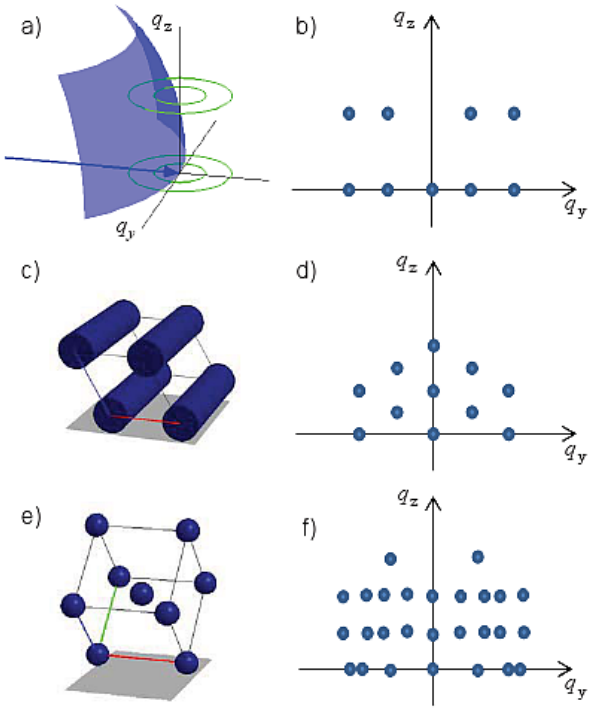

Figure 1: The geometry of a GISAXS experiment and examples of ordered mesoscale structures and their GISAXS patterns. a) A view of the reciprocal space of a "2D powder" structure, with rings of intensity (green) intersecting the Ewald sphere (purple). b) The image acquired by a detector during GISAXS measurements of the reciprocal space structure shown in (a). Where the rings of intensity in (a) intersect the Ewald sphere they are observed as spots on the detector. c, d) Hexagonally packed micellar "tubes" running parallel to the substrate, and the corresponding GISAXS pattern. e, f) Spherical micelles in a (110)-oriented body-centered cubic arrangment, and the corresponding GISAXS pattern.

(GISAXS), which is performed in reflection geometry. GISAXS reveals a 2D cross section of reciprocal space that facilitates identification of oriented nanostructures. Cf. Figure 1, which gives a sketch of the experimental geometry and the scattering patterns from selected ordered mesostructures. Figure 1a shows the beam entering along the q_y axis, with the semi-transparent sheet illustrating the Ewald sphere. Because of the cylindrical "2D powder" symmetry, the *hkl* reflections are smeared into rings of radius q_{xy}. For each ring that intersects the Ewald sphere, a diffraction spot appears on the detector, as seen in Figure 1b. Figure 1 also displays two structures that will be encountered in the following: Hexagonal packed micellar tubes (Figure 1c, d) and micelles in body centred cubic arrangements (Figure 1e, f).

In this study, we have prepared mesoporous alumina thin films and powders with pore sizes around 5 nm using triblock copolymers Pluronic P123 and Pluronic F127 and studied their mesostructure. The as-cast micellar films were studied by GISAXS combined with state-of-the-art data-analysis based on simulations. In addition to being of interest in their own right, organized aluminas might provide highly interesting support systems for studies of catalysts, as they provide a more well-defined environment for the catalytically active nanoparticles frequently having alumina as support. The tailored support materials may help to mask out pore-size effects encountered in catalyst characterization, and might thus lead to a better understanding of catalysis. Equally important, the monodisperse pore structure may lead to a new kind of thermally stable support materials.[7,8,19–21]

Experimental Section

Materials

Triblock copolymers Pluronic P-123 (MW = 5800 Da) and Pluronic F-127 (MW = 12500 Da) were purchased from BASF and used as surfactants in order to give pore sizes of approximately 3-5 nm in the final product.[10,22] The main difference between the surfactants is the length of the poly(ethylene glycol)-chain as shown in Figure 2.

Citric acid and nitric acid, ethanol, aluminium nitrate and aluminium sec-butoxide were purchased from Sigma-Aldrich and used as reducing agent, organic solvent and alumina precursors, respectively. In addition, catalyst precursor materials were purchased as metal acetyl acetonate, Me(acac), for cobalt and nickel from Sigma-Aldrich.

Sample Preparation

The synthesis was based on evaporation-induced self-assembly with a templating surfactant as introduced by J. Brinker *et al.*[23] A schematic of the self-assembly process is given in Figure 2.

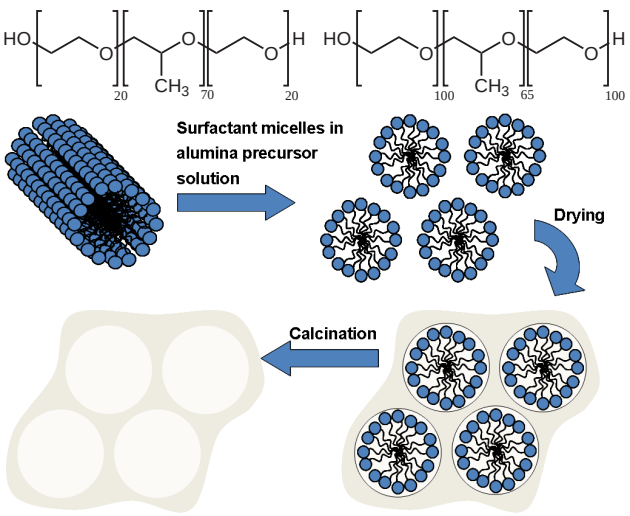

Figure 2: Chemical structure of the surfactants Pluronic P-123 (upper left structure) and Pluronic F-127 (upper right structure) and a schematic illustration of the preparation process. The surfactant, the alumina precursor and possible metal precursors are dissolved in an organic solvent. After the surfactant has self-assembled into ordered micelles and become immotile by the drying process, the organic residue is removed by calcination, resulting in a framework of ordered mesoporous alumina.

The generic synthesis procedure, adapted from Li *et al.*,[11] was to dissolve 1.0 g of surfactant in 20 mL of ethanol at room temperature (RT), adding 1.04 g of citric acid as reducing agent, 2.04 g (10 mmol) of aluminum nitrate, and metal acetyl acetonate (Me(acac), Me = Co, Ni). The amount of Me(acac) was varied, with the target value being 5 wt% of nickel and 11 wt% of cobalt with respect to the formed alumina. The mixture was stirred at room temperature (RT) for about 5 h and after two days of aging, the alumina sols were spin-coated (4000 rpm) on (100)-oriented Si wafers to obtain as-cast thin films for structural studies by X-ray scattering (GISAXS). The removal of the surfactant templates was done by calcination in air to form the final pore structure. Calcination was carried out by slowly increasing temperature from RT to 400 °C (1 °C/min ramping rate) and heating at 400 °C for 4 h in air.

Mesoporous alumina powders were prepared similarly to the thin films, meaning that all samples were prepared from F-127, ethanol, citric acid and aluminum nitrate in the same ratios as above, and without metal loadings. The main differences from the thin film preparation were the drying and calcination procedures. The temperature treatments for three chosen powder materials

Table 1: Overview of the organized mesoporous alumina (OMA) powder samples with variations in temperature treatment, all prepared using F-127 as templating agent.

Sample	**Conditions**	
	Drying	Calcination
OMA-fast	60 °C / 2 d	800 °C / 24 h
OMA-slow	30 °C / 6 d	500 °C / 24 h
OMA-medium	30 °C / 3 d	500 °C / 24 h
OMA-xrd	30 °C / 3 d	1000 °C / 24 h

are listed in Table 1. The samples are classified according to their drying procedure: the longest drying time was 6 days at 30 °C (OMA-slow), a medium drying time was 3 days at 30 °C (OMA-medium) and the shortest drying time was 2 days at 60 °C (OMA-fast). While standard alumina calcination was done at 500 °C, OMA-fast was treated at higher temperatures during drying and calcination (800 °C). The sample for the *in situ* powder X-ray diffraction (XRD) experiment was heated from RT to 1000 °C.

Grazing Incidence Small Angle X-ray Scattering (GISAXS)

GISAXS is utilized to study thin films and particles deposited on substrates. For incidence angles α_i less than a critical angle α_c, being about 0.2 ° for CuK_α, only the exponentially damped evanescent wave penetrates into the sample, thus giving a surface-sensitive technique for hard X-rays. GISAXS was performed at the Institute of Molecules and Materials of Le Mans (IMMM) on a Rigaku rotating copper anode working at 45 kV and 55 mA equipped with a confocal mirror producing an intense beam of X-rays collimated to 200 μm × 200 μm with a wavelength of 1.54 Å. The exposure time was 1000 seconds per frame and the incident angle was fixed to 0.20°. This angle is below the critical angle of the substrate so that the beam was penetrating the film without entering the silicon substrate, thus maximizing the scattering signal coming from the film itself. The distance from the sample to the 2D wire detector ("Gabriel" type[24]) was fixed to 83 cm and the detector pixel size was 150 μm. The scattering vector $\mathbf{q}$ is defined as the difference between the in- and outgoing wave vectors, $\mathbf{q} \equiv \mathbf{k_f} - \mathbf{k_i}$, and has magnitude $q = 4\pi \sin\theta/\lambda$ where θ is half the

total scattering angle 2θ. With the described setup, it was possible to access q up to 0.3Å^{-1}. We define q_x and q_y as the in-plane, and q_z as the out-of-plane, components of the scattering vector $\mathbf{q}$.

Calculating the scattering patterns is complicated because one generally cannot rely on the kinematic approximation, as refraction and multiple scattering effects become pronounced when both the incoming and scattered beams are near the critical angle. Further complications arise because the scattering objects generally are anisotropic and exhibit preferred orientation. We have previously published a framework for GIWAXS simulations,[25,26] which has recently been augmented to allow simulation of GISAXS patterns from substrate-supported film structures that are periodic in three dimensions.[27] The peak positions are calculated by the Laue conditions, taking into account material and geometric correction factors including the shift of the diffraction peaks due to refraction. The relative intensities of the reflections are obtained from the unit cell structure factor, accounting for the anisotropic form factor of the scattering objects. The film sample is assumed to consist of crystalline regions randomly oriented about the sample surface normal while having a well-defined crystallographic direction parallel to the surface normal, effectively constituting a '2D powder', as is consistent with the symmetry of all the experimental scattering patterns. Scattered intensity from the direct incoming beam and from the substrate-reflected incoming beam are summed - a procedure found to work well for relatively thick films. Static disorder was accounted for using a Debye-Waller factor. The patterns are on a logarithmic intensity scale, individually adjusted for readability.

In Situ X-ray Reflectivity

In situ X-ray reflectivity was carried out with a wavelength of 1.54 Å (Cu K_α) on a Panalytical Empyrean reflectometer at the IMMM working at 40 kV and 30 mA. The polychromatic beam coming from the copper anode was monochromatized and collimated by reflection on a multilayer mirror to obtain a parallel and monochromatic beam. The full width at half maximum (FWHM) of the direct beam was typically 0.06° with a peak intensity of the order of 5×10^7 counts/s. The size of the incident beam was about 15 mm $\times$ 100 μm. The detector was a Pixcel detector that was

used in the receiving slit mode using 3 channels in the vertical direction and 256 channels in the horizontal direction.

In Situ X-Ray Powder Diffraction

In situ X-ray powder diffraction was carried out on a Bruker D8 Advance instrument using Cu Kα radiation ($\lambda = 1.54$ Å) at 40 mA and 40 kV. A furnace was used to heat the sample from room temperature to 1000 ° C with a heating rate of 1.5 ° C per minute.

Focused Ion Beam - Scanning Electron Microscopy (FIB-SEM)

For the imaging experiments a Helios dual-beam FIB-SEM at NTNU Nanolab was used to cut and image a cross-section of the thin films. Before the SEM imaging, the samples were covered with a 30 nm thick gold layer and a carbon layer of dimensions $3 \times 15 \times 1$ μm. During the measurement a vacuum of 10^{-5} Pa was applied, the detector was at an angle of 52 ° and the SEM acceleration voltage was 50 keV.

N_2 Physisorption

Nitrogen physisorption was carried out with a Micromeritics TriStar II instrument at 77 K. After the samples were evacuated at 200 ° C for 12 h, the surface area was estimated with the Brunauer, Emmet and Teller (BET)[28] method in the relative pressure range 0.06–0.20. The average pore volume and pore size were estimated using the Barret, Joyner and Halenda (BJH) method, based on the nitrogen adsorption and desorption curves. The software used for the analysis was TriStar II 3020, version 1.03.

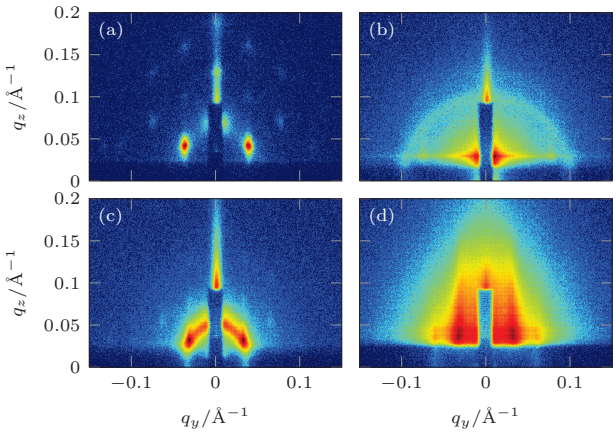

Figure 3: Experimental GISAXS patterns obtained from films prepared from P-123. a) As-cast film with alumina only, b) the same film after calcination to 400 °C, leading to a collapsed and essentially isotropic structure. c) As-cast film containing 11 wt% cobalt and 5 wt% nickel, d) the same film after calcination to 400 °C.

Results and Discussion

Films prepared from P-123

The prepared alumina sols readily self-assembled into highly ordered mesoscale structures, as judged from the numerous Bragg reflections seen in the GISAXS patterns. A thin film prepared from surfactant P-123, citric acid and aluminum nitrate gave reflections as shown in Figure 3a. The structure is consistent with a 2D hexagonal arrangement of the micelles. The missing reflections give important clues to the size of the micelles, as discussed later. Figure 3b shows that the structure becomes isotropic when calcined to 400 °C. During heat treatment the residues of solvent and surfactant are removed, which seems to destabilize the overall structural arrangement.

Also in the case of adding metal precursor to the sol, the GISAXS Bragg reflections show a hexagonal structure, as seen in Figure 3c. When the sample with 11 wt% cobalt and 5 wt% nickel was calcined to 400 °C features of the structure change qualitatively, but are still consistent with an anisotropic ordered structure (Figure 3d). The hexagonal 'tube' structure is evidently not stable enough to withstand the calcination. Albeit not maintaining the 3D micellar mesostructure, addition of the metal precursor seems to improve the stability, as judged from the more pronounced

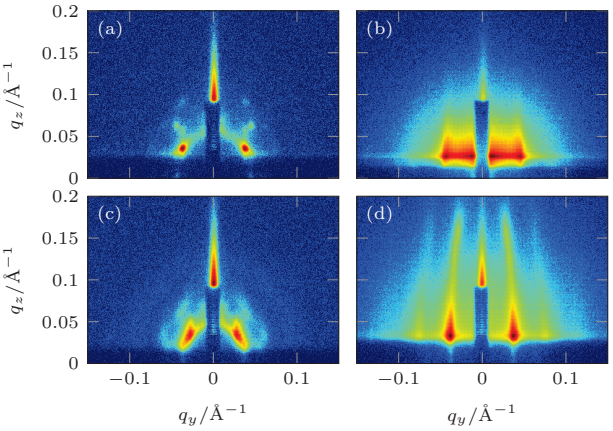

Figure 4: Experimental GISAXS patterns of samples prepared from F-127: (a) shows the as-cast film with alumina only and (b) with shows the film after calcination to 400 °C, leading to a strained structure. In (c) an as-cast sample is shown with addition 11 wt% cobalt and 5 wt% nickel, which in (d) was calcined to 400 °C.

GISAXS features for this film. A possible explanation could be that as the hydrophobic metal precursor is transfered into the the hydrophobic core of the surfactant micelles and consequently embedded into the pore-wall during calcination, thus stabilizing the pore structure.[11]

Films prepared from F-127

Even though the two surfactants P-123 and F-127 differ only in the chain length of their polymer blocks , the GISAXS patterns show that whereas P-123 gives hexagonal phases, using F-127 gives an essentially cubic structure with approximately spherical micelles. The GISAXS pattern in Figure 4a was measured from an uncalcined as-cast sample prepared from F-127 and is close to a body-centered cubic ($Im\bar{3}m$) structure with (110) orientation (the structure will be discussed in the following). This change in mesostructure is interesting also in terms of stability when removing the surfactant. While 2D hexagonal structures have long essentially tube-shaped pores which can easily collapse, 3D cubic structures tend to be more robust, as they have more stabilizing walls per column. This increased stability can be deduced from comparing the GISAXS patterns in Figure 3b and Figure 4b, in both cases showing calcined films without addition of metal precursors. The addition of metal loadings seems to improve the stability of the mesoporous structure upon

calcination for films prepared from F127. As shown in Figures 4c and 4d samples with 11 wt% cobalt and 5 wt% nickel were measured as-cast and after calcination with both samples exhibiting a perpendicular ordering. Compared to the calcined sample without addition of metal the reflections are more distinguishable, suggesting that more of the 3D structure induced by the micelles is maintained. Influences from an atomic-scale crystal structure were excluded as alumina from amorphous precursors is not becoming crystalline below 500 °C.[29]

Quantitative GISAXS Analysis

For the well-defined micellar (as-cast) films, our simulated GISAXS patterns are in excellent agreement with the experimental data, and allow extracting non-trivial information about the micelle size and shape from the experimental data. A series of fitted patterns is shown in Figure 5. Note that despite all the P-123 patterns shown being (close to) 2D hexagonal, there are significant differences in the relative intensities. The reflections therefore serve as "'fingerprints"' that can be used to assess the shape and size of the micelles.[27] It is particularly noteworthy that the subtle relative intensity variations for the P-123 samples are faithfully reproduced by the simulations. While the P-123 patterns are consistent with a pseudo-hexagonal 2D unit cell with long tubular micelles, the F-127 pattern can be understood as a (110)-oriented, vertically compressed, pseudo-bcc unit cell.

The main structural parameters varied to obtain the fits are listed in Table 2. In addition, an isotropic Debye-Waller factor of ~ 6 Å accounting for static disorder was employed. Peak broadening was introduced by assuming both an in-plane correlation length of ~ 700 Å and a crystal thickness limited to 8 unit cell repetitions along the sample normal. Uniaxial texture was included with a Gaussian of width 2° (FWHM). An important insight from the simulations is that the porous structures are substantially compressed (tens of percent) along the sample normal. For this reason, the 2D-pseudo-hexagonal structure (*p6mm*) of the P-123 films is more properly described by a two-micelle rectangular (planar group *c2mm*) unit cell, in the idealized hexagonal case having $a = a_{\mathrm{hex}}$ and $c = a_{\mathrm{hex}}\sqrt{3}/2$. Similarly, it can be shown that the (110)-oriented 3D-pseudo-cubic ($Im\bar{3}m$) structure can be described by a four-micelle face-centered orthorhombic (*Fmmm*) unit cell,

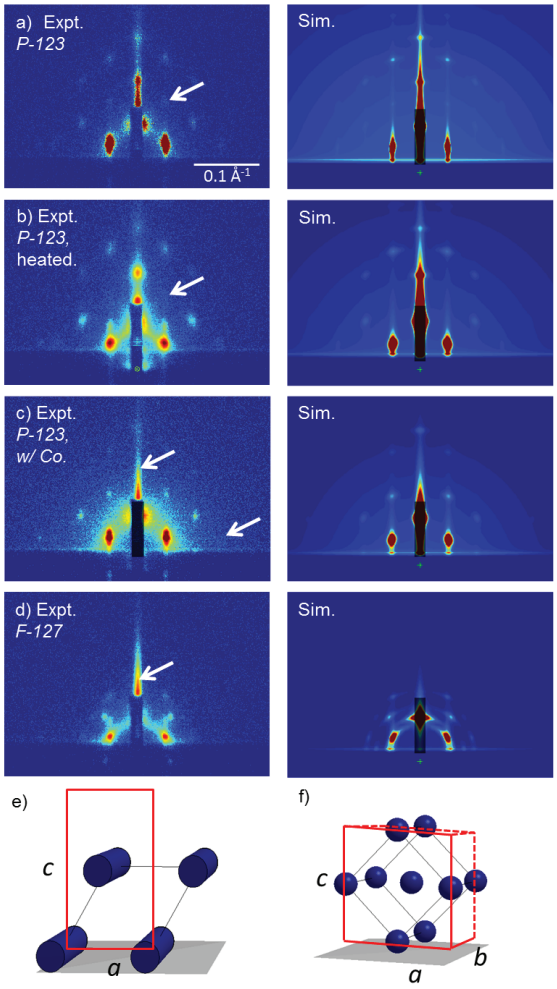

Figure 5: Comparisons of experimental and simulated GISAXS patterns: a) P-123 film, b) P-123 film after heat treatment to 80 °C, c) P-123 film with 9 wt% Co-loading, d) F-127 film. The arrows indicate Bragg reflections with strongly suppressed intensity because there are nearby deep minima of the scattering form factor of the micelles. The scale bar indicating the dimensions in reciprocal space is the same in all patterns shown. e) When the 2D hexagonal (*p6mm*) structure is vertically compressed, the structure becomes centered rectangular, *c2mm*, as indicated with the red frame. Note the elongated tubules, running parallel to the substrate. f) When the 3D body-centered cubic ($Im\bar{3}m$) structure is vertically compressed, the structure assumes a four-micelle *Fmmm* orthorhombic unit cell as indicated by the red cell.

Table 2: Structural parameters obtained from the scattering simulations. The incidence angle α_i was determined experimentally, and is thus not fitted. The radii denote the micelle dimensions along the (a), (b) and (c) directions.

	P-123	P-123 heated	P-123 w/Co	F-127
α_i / deg.	0.15	0.20	0.20	0.14
a / nm	16.9 ± 0.1	17.0 ± 0.1	16.4 ± 0.1	30.0 ± 0.3
b / nm	-	-	-	21.0 ± 0.3
c / nm	21.0 ± 0.1	20.0 ± 0.1	21.0 ± 0.1	22.5 ± 0.3
Elliptical	$R_a = 5.0 \pm 0.4$	$R_a = 5.0 \pm 0.2$	$R_a = 5.0 \pm 0.4$	-
cylinder / nm	$R_c = 3.5 \pm 0.2$	$R_c = 3.4 \pm 0.1$	$R_c = 3.5 \pm 0.1$	-
Spheroid / nm	-	-	-	$R_{ab} = 5.0 \pm 0.3$
	-	-	-	$R_c = 3.5 \pm 0.1$
Space group	*c2mm* (no. 9)	*c2mm* (no. 9)	*c2mm* (no. 9)	*Fmmm* (no. 69)

corresponding to the idealized cubic case when $a = c = a_{\text{cub}}\sqrt{2}$, and $b = a_{\text{cub}}$. Note that in both cases, we thus define the unit cell to have the *a*-*b* plane parallel to the substrate. After correcting for the non-negligible refraction, the small, yet non-negligible, corrections for refraction, the unit cell dimensions are directly given by the Bragg peak positions, yielding an accuracy of a few percent. The GISAXS pattern can be seen as the product of the anisotropic micelle form factors and structure factors, where the latter are given by the long range ordered lattice of micelles. Ultimately being a result of the high mono-dispersity of the micelles, the form factor of the micelles exhibit deep and sharp minima. If a minimum of the form factor thus happens to coincide with the position of a Bragg peak, the intensity of the Bragg peak will be strongly suppressed. For this reason, the uncertainty in some of the radii obtained through simulations is exceptionally low.[30] For the calcined mesoporous films, data analysis by GISAXS simulations was not carried out in the absence of a realistic mesostructure model.

In Situ Calcination

In order to follow the calcination process, during which the solvent, the surfactant and any other organic residue was removed, *in situ* X-ray reflectivity (XRR) experiments were performed. While

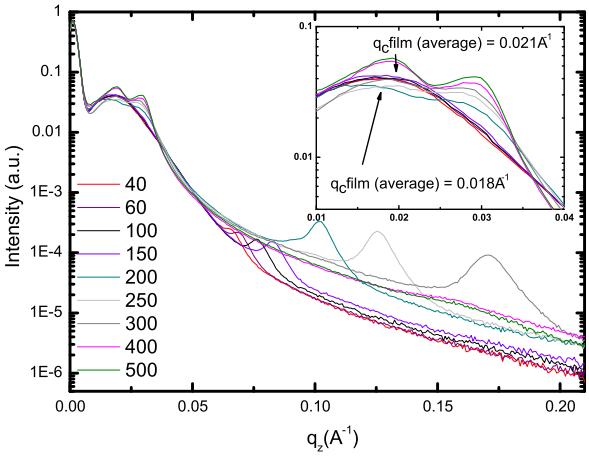

Figure 6: *In situ* X-ray reflectivity measurements with a F-127 sample heated up to 500 °C. With increasing temperature the Bragg peak moves from $q_z \approx 0.07$ Å^{-1} at 40 °C to $q_z \approx 0.17$ Å^{-1} at 500 °C, indicating a closer packing of the pores.

X-ray reflectivity is usually used to retrieve the electron density profile $\rho_e(z)$ from thin films, the high surface roughness of the films studied here precludes this kind of analysis, thus mainly giving information about the critical angle and the small-angle diffraction (Bragg) signal from periodicities in the film. Figure 6 shows specular scattering data from the calcination of a sol prepared from F-127, without metal loading. The changes in the reflectivity curves indicate the evaporation of the solvent (starting at ~ 60 °C) and of the surfactants (above 150 °C). The Bragg peak is the (002) reflection of the Fmmm structure, i.e., $c = 4\pi/q_z$, where c is twice the distance between close-packed micelles or pores. The Bragg peak moves towards higher q_z with increasing temperature. This peak is due to the periodic repetition along the film normal, and indicates a closer packing of the pores in the direction parallel to the sample normal with increasing temperature. Kiessig fringes are not observed in these measurements, presumably owing to the high surface roughness of ~ 16 nm also observed with atomic force microscopy (AFM; results not shown).

With FIB-SEM it is possible to sputter away material and cut a cross section into the film. An image of a calcined sample prepared from F-127 acquired using this technique is shown in Figure 7. The sample chosen for this technique is the calcined thin film prepared from F-127, with GISAXS pattern shown in Figure 4d. The image in Figure 7 shows a gold layer on top of the film to avoid charging problems during SEM imaging and a layer consisting of less structured alumina with the

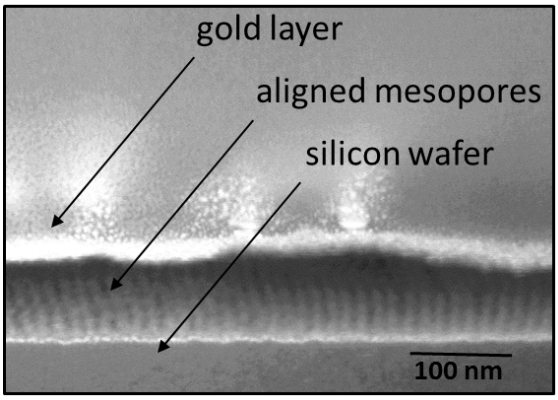

Figure 7: FIB-SEM images of the sample prepared from F-127 with addition of 11 wt% cobalt and 5 wt% nickel, after calcination. Arrays of pores oriented orthogonally with respect to the silicon wafer are clearly seen. The film thickness can be estimated around 100 nm.

aligned mesopores between the substrate and the top layer. The cross section reveals the rough surface of the film, with the overall film thickness estimated to be around 100 nm. The array of pores are oriented orthogonal with respect to the silicon wafer.

Powder Material

So far mesoporous alumina prepared as thin films and their characterization with GISAXS has been described. GISAXS is not applicable to powders and the studies of the mesoporous alumina powders were done by standard catalyst characterization techniques such as nitrogen physisorption and powder X-ray diffraction (XRD).

In order to follow the formation of an atomic-scale crystal structure *in situ* X-ray powder diffraction was performed. By calcining the sample from room temperature to 1000 °C while measuring XRD, it was determined at which temperature the amorphous organized alumina becomes crystalline. The results from the *in situ* experiment is presented in Figure 8. The phase transition from amorphous to crystalline alumina was found to occur at approximately 800 °C, as can be seen in the inset of Figure 8. A further increase of Bragg intensities at temperatures above 800 °C suggests that the crystallinity improves further with higher temperatures. This late formation of a crystal phase might be owing to amorphous alumina undergoing phase transitions in a rather acidic en-

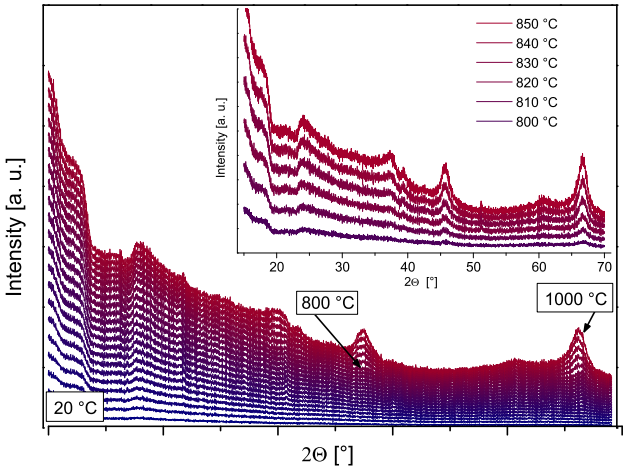

Figure 8: *In situ* diffractograms for monitoring the calcination process on OMA-xrd sample aquired using Cu K_α radiation. A diffractogram at every 50 ° C is shown from room temperature to 1000 ° C. The inset shows diffractograms from 800 ° C in steps of 10 ° C to show the phase transition from amorphous to crystalline alumina in detail. The diffractograms are displayed with a cumulative offset for clarity.

vironment (pH around 3 - 4).[29,31] The resulting crystal structure resembles the γ-alumina phase, commonly used as catalyst support material.

Nitrogen physisorption experiments using the Brunauer, Emmet and Teller (BET) method have been conducted to obtain information about the pore layout and surface area. The physisorption isotherms and hysteresis curves are shown in Figure 9a. Three versions of the organized mesoporous alumina (OMA) support are compared to each other and to commercial alumina purchased from Sasol (Puralox). All the materials display non-reversible adsorption-desorption isotherms with the desorption branches giving information about the pore entrance sizes. From the hysteresis loops for samples OMA-medium and OMA-slow it seems that the mesopore volume is constricted and depending on the size of the constriction desorption can occur via entrance size controlled pore blocking or by forced desorption due to cavitation. The isotherms of the standard alumina sample and OMA-fast display hysteresis loops expected for capillary condensation in mesopores. The difference in hysteresis loops indicates that OMA-medium and OMA-slow have more bottle-neck shaped pores. Desorption from open mesopores leads to parallel isotherm branches as seen in OMA-fast and the standard alumina sample.[32–34] The adsorption-desorption isotherms for OMA-medium and OMA-slow can be classified as type H4, according to IUPAC,[35] and indicate a meso-

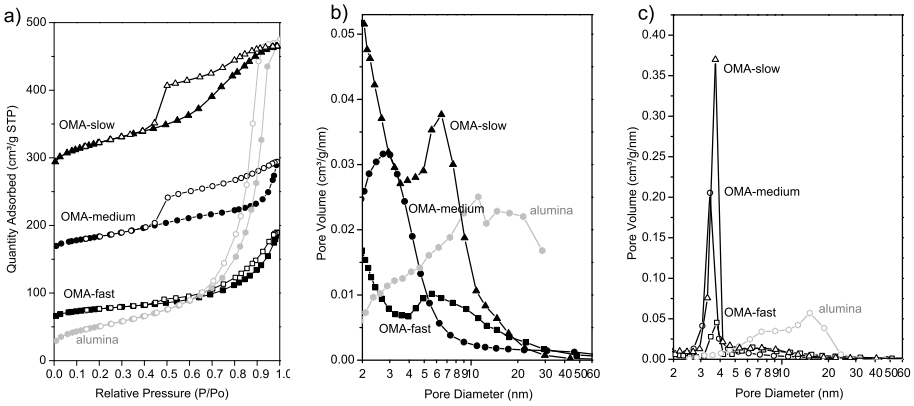

Figure 9: Nitrogen adsorption-desorption experiments on commercial alumina (gray lines) and samples of mesoporous alumina powder. a) Isotherms, offset for clarity by 50, 150 and 250 cm^3 STP/g. BJH pore size distribution estimated from adsorption isotherms (b) and desorption isotherms (c) by nitrogen physisorption.

porous material with good pore connectivity with a narrow distribution of complex, bottle-shaped pores present.[36,37] The hysteresis loops in the standard alumina sample and OMA-fast are of type H2[35] and suggests nearly tubular mesopores.

The corresponding pore size distributions, given in Figure 9b and Figure 9c, show that the pore structure withstands the calcination process as the average pore diameter of the support materials corresponds to pore diameters in the as-cast thin films. Compared to the wide size distribution in commercial alumina (5-30 nm), the samples exhibit an average pore size of 3 to 5 nm and show a maximal pore size distribution ranging from 3 to 10 nm. Sample OMA-slow gives the narrowest pore size distribution and the highest average pore size of the three samples. This can be seen more clearly in the pore size distribution calculated from the desorption branch of the isotherms (Figure 9c). The mean pore size values are smaller and around 4 nm, because of the difference in pore entrances and shape as seen from the hysteresis loops of the isotherms.

In addition, the BET measurements yield estimates for the surface area for all samples, which were high enough to show that the pores are stable throughout the synthesis and accessible from the gas phase. The highest surface area is exhibited by OMA-slow, 250 [m^2 / g], which also had the longest aging time. Accordingly, OMA-fast with the shortest aging time exhibits the smallest surface area, 90 [m^2 / g], and OMA-medium has an intermediate surface area of 120 [m^2 / g]. The

aging and calcination times seem to have an effect on the formed powder materials. The pores seem to be more organized and monodisperse with long aging times, based on pore size distribution and surface area calculated from the BET results. The powder becomes increasingly crystalline when calcined to temperatures above 800 °C, yet with higher temperatures the loss in monodispersity and surface area increases as well. The narrow pore size distribution between 3 and 5 nm suggests that organization of the pores, induced by close packing of the micelles, is present also in the powders.

Conclusions

Synthesis of highly ordered thin mesostructured alumina films was achieved via evaporation-induced self-assembly. It proved possible to synthesize alumina thin films with different ordered micelle structures, yet with varying degree of thermal stability. Structural studies of the thin films were focused on the mesoscale ordering inside the films using GISAXS, XRR and FIB-SEM, revealing that several packing motifs were present in the films, depending on the surfactants and processing conditions. Films prepared from P-123 show a (pseudo-)hexagonal structure with long tubular micelles, however with low thermal stability. Films prepared from F-127 gave a (pseudo-)cubic arrangement of spheroidal micelles, and the films calcined to 400 °C still exhibited indications of regular internal structures. State-of-the-art simulations of GISAXS patterns demonstrate that the micelles in all the as-cast films were vertically compressed, and with size of 3 to 5 nm. The calcined films gave GISAXS patterns consistent with internal mesoscale order, presumably in the form of a mesoporous network. Mesoporous alumina powder was synthesized as an important step towards the application as catalyst support material. The powder material exhibits a nearly uniform pore size between 3 and 5 nm, and a relatively high surface area of 250 [m^2 / g], thus paving the way to more well-defined support materials.

Acknowledgement

The authors thank Per Erik Vullum for doing FIB-SEM at NTNU Nanolab and Karin Wiggen Dragsten at the KINCAT group at NTNU. This work was supported by the French-Norwegian exchange program Aurora, through The Research Council of Norway (NFR) and the French ministry of reserach (MESR). We also acknowledge funding from NFR for the national infrastructure Resource Center for X-ray Scattering and Imaging (RECX), and Strategic Area Materials at NTNU for seed funding this project. Tthe authors would also like to thank NFR for financial support through the KOSK-II and SYNKROTRON programmes.

References

(1) Kresge, C. T.; Leonowicz, M. E.; Roth, W. J.; Vartuli, J. C.; Beck, J. S. Ordered mesoporous molecular sieves synthesized by a liquid-crystal template mechanism. *Nature (London, United Kingdom)* **1992**, *359*, 710–12.

(2) Walcarius, A.; Sibottier, E.; Etienne, M.; Ghanbaja, J. Electrochemically assisted self-assembly of mesoporous silica thin films. *Nature Materials* **2007**, *6*, 602–608.

(3) Kang, T.-S.; Smith, A. P.; Taylor, B. E.; Durstock, M. F. Fabrication of Highly-Ordered TiO2 Nanotube Arrays and Their Use in Dye-Sensitized Solar Cells. *Nano Letters* **2009**, *9*, 601–606.

(4) Buttard, D.; Schuelli, T.; Lazzari, R. Structural investigation of nanoporous alumina film with grazing incidence small angle X-ray scattering. *Physica Status Solidi A: Applications and Materials Science* **2013**, *210*, 2521–2525.

(5) Cai, W.; Yu, J.; Anand, C.; Vinu, A.; Jaroniec, M. Facile Synthesis of Ordered Mesoporous Alumina and Alumina-Supported Metal Oxides with Tailored Adsorption and Framework Properties. *Chemistry of Materials* **2011**, *23*, 1147–1157.

(6) Yuan, Q.; Yin, A.-X.; Luo, C.; Sun, L.-D.; Zhang, Y.-W.; Duan, W.-T.; Liu, H.-C.; Yan, C.-H. Facile Synthesis for Ordered Mesoporous gamma-Aluminas with High Thermal Stability. *Journal of the American Chemical Society* **2008**, *130*, 3465–3472.

(7) Borg, O.; Eri, S.; Blekkan, E. A.; Storsaeter, S.; Wigum, H.; Rytter, E.; Holmen, A. Fischer-Tropsch synthesis over gamma-alumina-supported cobalt catalysts: Effect of support variables. *Journal of Catalysis* **2007**, *248*, 89–100.

(8) Enger, B. C.; Fossan, A.-L.; Borg, O.; Rytter, E.; Holmen, A. Modified alumina as catalyst support for cobalt in the Fischer-Tropsch synthesis. *Journal of Catalysis* **2011**, *284*, 9–22.

(9) Swaddle, T. W.; Rosenqvist, J.; Yu, P.; Bylaska, E.; Phillips, B. L.; Casey, W. H. Kinetic Evidence for Five-Coordination in AlOH(aq)2+ Ion. *Science (Washington, DC, United States)* **2005**, *308*, 1450–1453.

(10) Ha, T.; Park, H.; Kang, E. S.; Shin, S.; Cho, H. H. Variations in mechanical and thermal properties of mesoporous alumina thin films due to porosity and ordered pore structure. *Journal of Colloid and Interface Science* **2010**, *345*, 120–124.

(11) Li, Z.-X.; Shi, F.-B.; Li, L.-L.; Zhang, T.; Yan, C.-H. A facile route to ordered mesoporous-alumina-supported catalysts, and their catalytic activities for CO oxidation. *Physical Chemistry Chemical Physics* **2011**, *13*, 2488–2491.

(12) Jiang, X.; Oveisi, H.; Nemoto, Y.; Suzuki, N.; Wu, K. C.-W.; Yamauchi, Y. Synthesis of highly ordered mesoporous alumina thin films and their framework crystallization to gamma-alumina phase. *Dalton Transactions* **2011**, *40*, 10851–10856.

(13) Lesaint, C.; Glomm, W. R.; Borg, O.; Eri, S.; Rytter, E.; Oye, G. Synthesis and characterization of mesoporous alumina with large pore size and their performance in Fischer-Tropsch synthesis. *Applied Catalysis, A: General* **2008**, *351*, 131–135.

(14) Kuemmel, M.; Grosso, D.; Boissiere, C.; Smarsly, B.; Brezesinski, T.; Albouy, P. A.; Amenitsch, H.; Sanchez, C. Thermally stable nanocrystalline gamma-alumina layers with highly ordered 3D mesoporosity. *Angewandte Chemie, International Edition* **2005**, *44*, 4589–4592.

(15) Weidmann, C.; Brezesinski, K.; Suchomski, C.; Tropp, K.; Grosser, N.; Haetge, J.; Smarsly, B. M.; Brezesinski, T. Morphology-Controlled Synthesis of Nanocrystalline eta-Al2O3 Thin Films, Powders, Microbeads, and Nanofibers with Tunable Pore Sizes from Preformed Oligomeric Oxo-Hydroxo Building Blocks. *Chemistry of Materials* **2012**, 486–494.

(16) Caragheorgheopol, A.; Rogozea, A.; Ganea, R.; Florent, M.; Goldfarb, D. Investigation of the Surfactant Role in the Synthesis of Mesoporous Alumina. *J. Phys. Chem. C* **2009**, *114*, 28–35.

(17) Tate, M. P.; Hillhouse, H. W. General Method for Simulation of 2D GISAXS Intensities for Any Nanostructured Film Using Discrete Fourier Transforms. *Journal of Physical Chemistry C* **2007**, *111*, 7645–7654.

(18) Tanaka, S.; Tate, M. P.; Nishiyama, N.; Ueyama, K.; Hillhouse, H. W. Structure of Mesoporous Silica Thin Films Prepared by Contacting PEO106-PPO70-PEO106 Films with Vaporized TEOS. *Chemistry of Materials* **2006**, *18*, 5461–5466.

(19) Rotan, M.; Rytter, E.; Einarsrud, M.-A.; Grande, T. Solid state mechanism leading to enhanced attrition resistance of alumina based catalyst supports for Fischer-Tropsch synthesis. *Journal of the European Ceramic Society* **2013**, *33*, 1–6.

(20) Borg, O.; Dietzel, P. D. C.; Spjelkavik, A. I.; Tveten, E. Z.; Walmsley, J. C.; Diplas, S.; Eri, S.; Holmen, A.; Rytter, E. Fischer-Tropsch synthesis: Cobalt particle size and support effects on intrinsic activity and product distribution. *Journal of Catalysis* **2008**, *259*, 161–164.

(21) Xiong, H.; Zhang, Y.; Wang, S.; Li, J. Fischer-Tropsch synthesis: the effect of Al2O3 porosity on the performance of Co/Al2O3 catalyst. *Catalysis Communications* **2005**, *6*, 512–516.

(22) Dourdain, S.; Bardeau, J.-F.; Colas, M.; Smarsly, B.; Mehdi, A.; Ocko, B. M.; Gibaud, A. Determination by x-ray reflectivity and small angle x-ray scattering of the porous properties of mesoporous silica thin films. *Applied Physics Letters* **2005**, *86*, 113108/1–113108/3.

(23) Brinker, C. J.; Lu, Y.; Sellinger, A.; Fan, H. Evaporation-induced self-assembly. Nanostructures made easy. *Advanced Materials (Weinheim, Germany)* **1999**, *11*, 579–585.

(24) Gabriel, A.; Dauvergne, F.; Rosenbaum, G. Linear, circular and two dimensional position sensitive detectors. *Nuclear Instruments & Methods* **1978**, *152*, 191–4.

(25) Breiby, D. W.; Bunk, O.; Andreasen, J. W.; Lemke, H. T.; Nielsen, M. M. Simulating X-ray diffraction of textured films. *Journal of Applied Crystallography* **2008**, *41*, 262–271.

(26) Breiby, D. W.; Chin, P. T. K.; Andreasen, J. W.; Grimsrud, K. A.; Di, Z.; Janssen, R. A. J. Biaxially Oriented CdSe Nanorods. *Langmuir* **2009**, *25*, 10970–10974.

(27) Panduro, E. A. C.; Granlund, H.; Sztucki, M.; Konovalov, O.; Breiby, D. W.; Gibaud, A. Using Three-Dimensional 3D Grazing-Incidence Small-Angle X-ray Scattering (GISAXS) Analysis To Probe Pore Deformation in Mesoporous Silica Films. *ACS Applied Materials & Interfaces* **2014**, *6*, 2672–2677.

(28) Barrett, E. P.; Joyner, L. G.; Halenda, P. P. The determination of pore volume and area distributions in porous substances. I. Computations from nitrogen isotherms. *Journal of the American Chemical Society* **1951**, *73*, 373–80.

(29) Levin, I.; Brandon, D. Metastable alumina polymorphs: crystal structures and transition sequences. *Journal of the American Ceramic Society* **1998**, *81*, 1995–2012.

(30) Boissiere, C.; Grosso, D.; Lepoutre, S.; Nicole, L.; Bruneau, A. B.; Sanchez, C. Porosity and Mechanical Properties of Mesoporous Thin Films Assessed by Environmental Ellipsometric Porosimetry. *Langmuir* **2005**, *21*, 12362–12371.

(31) Wang, J. A.; Bokhimi, X.; Morales, A.; Novaro, O.; Lopez, T.; Gomez, R. Aluminum Local Environment and Defects in the Crystalline Structure of Sol-Gel Alumina Catalyst. *Journal of Physical Chemistry B* **1999**, *103*, 299–303.

(32) Eggenhuisen, T. M.; Zecevic, J.; Talsma, H.; de, K. P., Jong; de, P. E., Jongh Quantitative Assessment of Pore Blockage in Supported Catalysts: Comparing Differential Scanning Calorimetry and Physisorption. *Journal of Physical Chemistry C* **2012**, *116*, 7480–7490.

(33) Eggenhuisen, T. M.; Prieto, G.; Talsma, H.; de, K. P., Jong; de, P. E., Jongh Entrance Size Analysis of Silica Materials with Cagelike Pore Structure by Thermoporometry. *Journal of Physical Chemistry C* **2012**, *116*, 23383–23393.

(34) Martinez, A.; Prieto, G.; Rollan, J. Nanofibrous gamma-Al2O3 as support for Co-based Fischer-Tropsch catalysts: Pondering the relevance of diffusional and dispersion effects on catalytic performance. *Journal of Catalysis* **2009**, *263*, 292–305.

(35) Sing, K. S. W. Reporting physisorption data for gas/solid systems with special reference to the determination of surface area and porosity (Recommendations 1984). *Pure and Applied Chemistry* **1985**, *57*, 603–619.

(36) Kaneko, K. Determination of pore size and pore size distribution 1. Adsorbents and catalysts. *Journal of Membrane Science* **1994**, *96*, 59–89.

(37) Morishige, K.; Tateishi, M.; Hirose, F.; Aramaki, K. Change in Desorption Mechanism from Pore Blocking to Cavitation with Temperature for Nitrogen in Ordered Silica with Cagelike Pores. *Langmuir* **2006**, *22*, 9220–9224.

Graphical TOC Entry